



# Numerical studies on four-engine rocket exhaust plume impinging on flame deflectors with afterburning

Zhi-tan Zhou, Chang-fang Zhao, Chen-yu Lu, Gui-gao Le<sup>\*</sup>

School of Mechanical Engineering, Nanjing University of Science and Technology, Nanjing, 210094, China

## ARTICLE INFO

### Article history:

Received 21 January 2020

Received in revised form

1 June 2020

Accepted 16 June 2020

Available online 30 June 2020

### Keywords:

Four-engine rocket

Afterburning

Impinging flow field

Different deflectors

Numerical simulations

## ABSTRACT

This paper studies the four-engine liquid rocket flow field during the launching phase. Using three-dimensional compressible Navier-Stokes equations and two-equation realizable k-epsilon turbulence model, an impact model is established and flow fields of plume impinging on the two different shapes of flame deflectors, including wedge-shaped flame deflector and cone-shaped flame deflector, are calculated. The finite-rate chemical kinetics is used to track chemical reactions. The simulation results show that afterburning mainly occurs in the mixed layer. And the region of peak pressure occurs directly under the rocket nozzle, which is the result of the direct impact of exhaust plume. Compared with the wedge-shaped flame deflector, the cone-shaped flame deflector has great performance on guiding exhaust gas. The wedge-shaped and cone-shaped flame deflectors guide the supersonic exhaust plume away from the impingement point with two directions and circumferential direction, respectively. The maximum pressure and temperature on the wedge-shaped flame deflector surface are 37.2% and 9.9% higher than those for the cone-shaped flame deflector. The results provide engineering guidance and theoretical significance for design in flame deflector of the launch platforms.

© 2020 China Ordnance Society. Publishing services by Elsevier B.V. on behalf of KeAi Communications Co. Ltd. This is an open access article under the CC BY-NC-ND license (<http://creativecommons.org/licenses/by-nc-nd/4.0/>).

## 1. Introduction

To explore the further deep space, many countries are developing new generation launch vehicles with more effective loads. Particularly, the heavy-lift capability launch vehicle is the focus of recent research in many space programs [1,2]. To achieve a large carrying capacity, the propulsion systems usually use multiple engines working simultaneously to improve the launch power [3,4]. The multi-engine rockets have certain advantages by comparing with the single-engine rocket, but the impingement flow field is more complex, which caused by the exhaust plume interaction [5]. The jet flow impingement has been the vital factor for the launch safety. Since the rocket engines are close to the launch platform during launching phase, the exhaust jets of rocket engine not only disturb the attitude of rocket in the take-off, but also have a thermal impact on the rocket base and ground control system. Therefore, the jet flow characteristics of multi-engine rockets exhaust plume need to be studied carefully for the risk

aversion and improvement of achievement ratio in launching [6–9].

During rocket launching, the exhaust gas impingement induces large aerothermodynamic and acoustic loads on the launch platform [10,11]. To reduce the effect of thermal shock and dynamic of the rocket jet flow, flame deflectors have been installed under the rocket engine to guide the exhaust gas of high temperature and velocity away from the channel without recirculation. It is generally known that the shape of deflector surface is the main factor affecting the diversion performance of the flame deflector. The flame deflector structure should be designed to restrain the exhaust plume from backdraft inside the deflector and to protect the rocket from damage of discharged gas during launching [12]. The poor efficiency of diversion can cause blockage of the deflector channel by the recirculation flow. The accumulation and reflection of the high temperature gas have a negative influence on the stability of the flame deflector and security of the launch process. Using the reasonable shape of the flame deflector can reduce the adverse effects caused by the recirculation or backdraft of rocket exhaust gas [13–15]. For these reasons, studying the diversion efficiency of different shapes of flame deflector is important for the safety of launch.

<sup>\*</sup> Corresponding author.

E-mail address: [leguigao@njjust.edu.cn](mailto:leguigao@njjust.edu.cn) (G.-g. Le).

Peer review under responsibility of China Ordnance Society

### Nomenclature

$A_r$	preexponential factor for reaction step $r$
$C_i$	molar concentration of species $i$
$E_{Ar}$	activation energy of reaction step $r$
$D_e$	nozzle-exit diameter
$D_s$	diameter of circle through nozzle centerline
$D_a$	throat diameter
$L$	axis length of nozzle
$M_i$	chemical symbol of species $i$
$P$	environment pressure
$T$	environment temperature
$Y_i$	the local mass fraction of species $i$
$\mu$	viscosity coefficient
$e$	specific kinetic energy
$\rho$	fluid density
$\tau$	stress
$g_i$	Gibbs free energy of $i$

With the rapid development of computational facilities and technology, numerical simulations have been utilized more widely in the aerospace science and technology. In addition, the significant experimental cost savings can be realized. Extensive studies on shock characteristics of the launch vehicle exhaust gas have been conducted numerical simulations and launch tests in the past decades. Daniel and Vineet [16] obtained the structure of the ARES V exhaust jet flow and its impingement characteristics on the B-2 flame deflector by using a multi-element flow solver. The results

showed that significant reversed flows can be developed on the flame deflector surface due to the larger impingement angle and associated detached flame deflector shock wave. Sachdev et al. [17] investigated the temperature load on the flame deflector by numerical simulations. The efficiency and accuracy of the methodology was verified through its application in an actual sub-scale test facility. Tsutsumi et al. [18] developed a universal performance assessment and control system-large eddy simulation (UPACS-LES) computational code to study the effect of deflector shape on the plate and the tail shock waves. It showed that the magnitude of the plate shock and acoustic level around the vehicle were weakened by employing steeply inclined deflector plane. Jiang et al. [10] presented an overview on progresses and perspectives of the jet impingement research for rocket launching. A summary of the interactive mechanisms between impinging jets and the launch platform or the flame deflector system was provided.

The studies above have provided reference and help for the analysis of the engine exhaust impinging on the launch structures, and several dynamics mechanisms are studied separately or in a partially-coupled way. Still, there are many problems about the exhaust jet impingement on different flame deflectors remaining to be solved, especially when considering afterburning effect. This paper studies the influences of two shapes of flame deflector configurations which are designed for the four-engine liquid rockets. A comparison of the rocket motor exhaust jet impingement on the different deflectors can reflect the variation of flow field and provides reference for designs of the launch platforms.

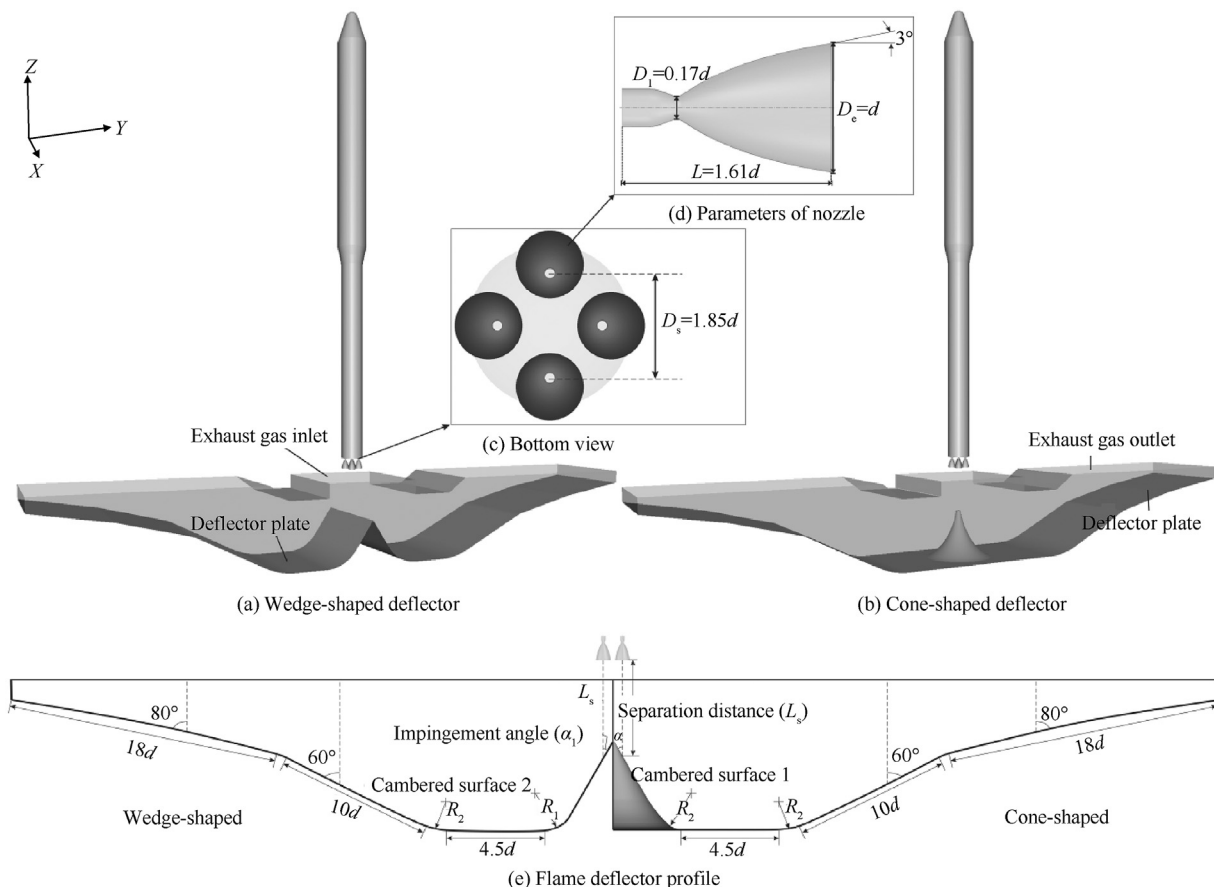


Fig. 1. Computational fluid dynamics models.

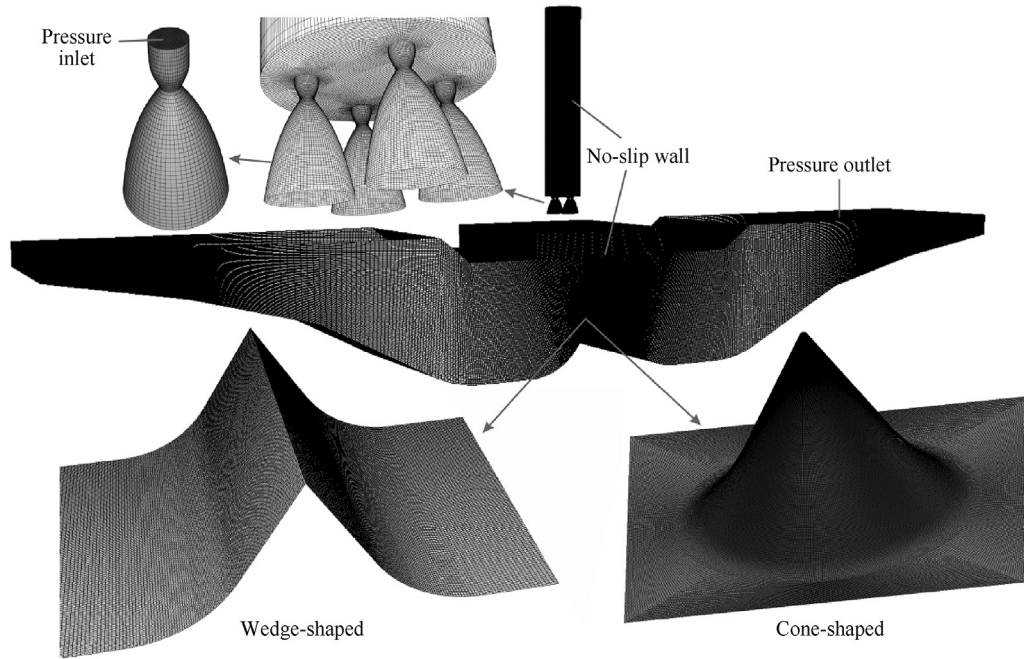


Fig. 2. Computational grid and boundary conditions.

## 2. Four-engine rocket model

### 2.1. Geometric model of the platform

The system of this study is a three-stage liquid rocket which utilizes kerosene/liquid oxygen (LOX) propellant as propulsion system for the first stage. Fig. 1(a) and (b) show the structures of the four-engine rocket with the wedge-shaped and cone-shaped deflectors. Fig. 1(c) displays the installation positions of four nozzles. The four Laval nozzles are identical in geometry. As shown in Fig. 1(d), the Laval nozzle has an exit half-angle of  $3^\circ$ , a nozzle spacing ratio ( $D_s/D_e$ ) of 1.82, and a nozzle expansion ratio ( $D_t/D_e$ ) of 0.17. As shown in Fig. 1(e), the structure of the two deflectors is identical except for the shapes of positive impulse area, which are the wedge and cone, respectively. The separation distance ( $L_s$ ) between the nozzle exit and the deflector surface is  $5d$ , which  $d$  corresponds to the nozzle exit diameter. The appropriate jet impingement angle shall minimize the induced thermal shock loading on the rocket. Therefore, an impingement angle ( $\alpha_1$ ) of  $30^\circ$  is used in the deflector design [19]. The exit radius of the cambered surface 1 and 2 are 2 and 1.5 times of the nozzle exit, respectively. More parameters of the deflectors are shown in the flame deflector profiles.

### 2.2. Computational grids

Structured mesh with tensor product structure has better numerical ability than unstructured grids using a multi-block. Also structured mesh can improve the fidelity of the flow solutions and assure a good resolution of shock waves in the flow field, the computational mesh of this paper is shown in Fig. 2. No-slip adiabatic temperature condition is applied for the solid walls of the

rocket and deflectors. The inlet condition is set as the total temperature 3800 K and the total pressure 18.66 MPa. The species mole fractions of exhaust gas at inlet are given in Table 1.

## 3. Numerical method

### 3.1. Governing equations

The liquid rocket exhaust is considered as an ideal gas mixture with the continuum assumption. The numerical solution of the compressible, Reynolds-averaged Navier-Stokes (RANS) methods has been obtained by using second-order total variation diminishing (TVD) schemes with finite volume method [20]. The simulations in this paper were performed using CFD++ software. The multi-component conservation equation takes the following form

$$\frac{\partial}{\partial t}(\rho Y_i) + \nabla \cdot (\rho v Y_i) = -\nabla \cdot \mathbf{J}_i + R_i + S_i \quad (1)$$

where  $S_i$  is the rate of creation by addition from the dispersed phase. The diffusion flux  $\mathbf{J}_i$  is defined as

$$\nabla \cdot \mathbf{J}_i = -\rho D_{i,m} \nabla Y_i - D_{T,i} \frac{\nabla T}{T} \quad (2)$$

The governing equations for mass, momentum, and energy conservations for each species are given as follows:

$$\frac{\partial \mathbf{U}}{\partial t} + \frac{\partial (\mathbf{F} - \mathbf{F}_v)}{\partial x} + \frac{\partial (\mathbf{G} - \mathbf{G}_v)}{\partial y} + \frac{\partial (\mathbf{H} - \mathbf{H}_v)}{\partial z} = 0 \quad (3)$$

Table 1

The composition and content of exhaust gas at the nozzle inlet.

Component	H <sub>2</sub> O (vapor)	CO <sub>2</sub>	CO	H <sub>2</sub>	Air
Mole fraction	0.39	0.26	0.25	0.09	0.01

$$\begin{cases} \mathbf{U} = (\rho, \rho u, \rho v, \rho w, \rho e)^T \\ \mathbf{F} = (\rho u, \rho u^2 + p, \rho uv, \rho uw, \rho u(e + p/\rho))^T \\ \mathbf{G} = (\rho v, \rho uv, \rho v^2 + p, \rho vw, \rho v(e + p/\rho))^T \\ \mathbf{H} = (\rho w, \rho uw, \rho vw, \rho w^2 + p, \rho w(e + p/\rho))^T \end{cases} \quad (4)$$

$$\begin{cases} \mathbf{F}_v = (0, \tau_{xx}, \tau_{xy}, u\tau_{xx} + v\tau_{xy} + w\tau_{xz} + K\partial T/\partial x)^T \\ \mathbf{G}_v = (0, \tau_{yx}, \tau_{yy}, u\tau_{xy} + v\tau_{yy} + w\tau_{yz} + K\partial T/\partial y)^T \\ \mathbf{H}_v = (0, \tau_{zx}, \tau_{zy}, u\tau_{xz} + v\tau_{yz} + w\tau_{zz} + K\partial T/\partial z)^T \end{cases} \quad (5)$$

$$\begin{cases} \tau_{xx} = \frac{2}{3}\mu(2u_x - v_y - w_z) \\ \tau_{yy} = \frac{2}{3}\mu(2v_y - u_x - w_z), \begin{cases} \tau_{xy} = \mu(2u_y + v_x) \\ \tau_{xz} = \mu(2u_z + w_x) \\ \tau_{yz} = \mu(2v_z + w_y) \end{cases} \\ \tau_{zz} = \frac{2}{3}\mu(2w_z - u_x - v_y) \end{cases} \quad (6)$$

where  $\mathbf{U}$  is the flow variables,  $\mathbf{F}$ ,  $\mathbf{G}$ ,  $\mathbf{H}$  are the flow flux vectors, and  $\mathbf{F}_v$ ,  $\mathbf{G}_v$ ,  $\mathbf{H}_v$  are the viscous flux vectors.

### 3.2. Turbulence model

The supersonic jet impingement on deflector was computed using the realizable  $k$ - $\varepsilon$  turbulence model, which has been used for solving the flow field near the wall [21]. The transport equations for turbulence kinetic energy,  $k$  and its rate of dissipation,  $\varepsilon$  in the realizable  $k$ - $\varepsilon$  model are given as

$$\frac{\partial(\rho k)}{\partial t} + \frac{\partial(\rho k u_i)}{\partial x_i} = \frac{\partial}{\partial x_j} \left[ \left( \mu + \frac{\mu_t}{\sigma_k} \right) \frac{\partial k}{\partial x_j} \right] + G_k - \rho \varepsilon \quad (7)$$

and

$$\frac{\partial(\rho \varepsilon)}{\partial t} + \frac{\partial(\rho \varepsilon u_i)}{\partial x_i} = \frac{\partial}{\partial x_j} \left[ \left( \mu + \frac{\mu_t}{\sigma_\varepsilon} \right) \frac{\partial \varepsilon}{\partial x_j} \right] + \rho C_1 E \varepsilon - \rho C_2 \frac{\varepsilon^2}{k + \sqrt{\nu \varepsilon}} \quad (8)$$

In Eqs. (7) and (8),  $G_k$  is the generation of turbulence kinetic energy due to the mean velocity gradients. The model constants  $C_1$  and  $C_2$  are 1.44 and 1.9 respectively.

### 3.3. Reaction model

As the fuel burns, gases expand to fill the combustion chamber and create a high pressure. Meanwhile, the unstable components such as CO and  $H_2$  are emitted. The fuel-rich exhaust gas from the nozzle exit mixes with the ambient atmosphere, and this may lead to afterburning reaction. To ensure the reliability and accuracy of the numerical result, the finite-rate chemical kinetics is used to

**Table 3**

The parameters of freestream at 5, 15, 25, and 25 km.

Altitudes/km	Pressure/Pa	Temperature/K	Mach number
5	54052	256	0.52
15	12540	220	1.39
25	2549	222	2.24
35	575	237	3.06

track chemical reaction system. This method, which based on the Law of Mass Action [22], is applied to calculate the various steps of the chemical mechanism [23].

The general chemical reaction  $r$  is given by

$$\sum_i v_{ir}' M_i = \sum_i v_{ir}'' M_i \quad (9)$$

In Eq. (9),  $v_{ir}'$  and  $v_{ir}''$  are the stoichiometric coefficients of species  $i$  in reactant and product side of step  $r$ , and the rate of production of species  $i$  from the reaction step  $r$  can be written as follows

$$\omega_{ir} = W_i (v_{ir}'' - v_{ir}') \left[ K_{fr} \prod_m C_m^{v_{ir}'} - K_{br} \prod_m C_m^{v_{ir}''} \right] \quad (10)$$

where  $K_{fr}$  and  $K_{br}$  are the forward and backward rate constant for reaction  $r$  respectively. The forward rate constant for each reaction step  $r$  is given by Arrhenius kinetics

$$K_{fr} = A_r T^{N_r} \exp\left(\frac{-E_{Ar}}{R_0 T}\right) \left(\frac{P}{P_{atm}}\right)^{N_p} \quad (11)$$

Here,  $N_r$  and  $N_p$  are exponents of temperature in the rate constant of reaction  $r$ , the backward rate constant  $K_{br}$  is computed from the equilibrium condition

$$\frac{K_{fr}}{K_{br}} = \left(\frac{P_{atm}}{R_0 T}\right)^{\sum_i (v_{ir}'' - v_{ir}')} \exp\left(\frac{-\Delta \bar{G}_r}{R_0 T}\right) \quad (12)$$

The change in Gibbs free energy  $\Delta \bar{G}$  for reaction step  $r$  is given by

$$\Delta \bar{G}_r = \sum_{i=1}^N v_{ir}'' W_i g_i - \sum_{i=1}^N v_{ir}' W_i g_i \quad (13)$$

The exhaust gas in the afterburning reactions includes  $H_2O$ ,  $H_2$ ,  $O_2$ ,  $CO_2$ ,  $CO$ , and  $N_2$ , with  $H$ ,  $O$ , and  $OH$  as the free radicals of the intermediate products in combustion. Therefore, the 9-species and 14-step chemical mechanism is employed for  $H_2/CO$  afterburning [24] as shown in Table 2.

## 4. Model validation

The Mach number contours on the symmetry plane at different flight altitudes are obtained by numerical method described above. The total pressure and temperature in the chamber are 18.66 MPa

**Table 2**

Reaction mechanism of hydrogen and carbon monoxide.

NO.	Reaction	$A_r$	$N_T$	$E_{Ar}$	NO.	Reaction	$A_r$	$N_T$	$E_{Ar}$
<b>R1a</b>	$H_2 + O = OH + H$	3.82(9)	0.000	3.33(7)	<b>R7</b>	$O + O + M_1 = O_2 + M_1$	5.40(7)	0.000	-7.60(6)
<b>R1b</b>	$H_2 + O = OH + H$	1.03(12)	0.000	8.02(7)	<b>R8</b>	$H + OH + M_3 = H_2O + M_3$	5.56(16)	-2.000	0.00
<b>R2</b>	$H + O_2 = OH + O$	2.07(11)	-0.097	6.29(7)	<b>R9a</b>	$CO + OH = CO_2 + H$	1.00(10)	0.000	6.69(7)
<b>R3</b>	$OH + H_2 = H_2O + H$	2.17(5)	1.520	1.45(7)	<b>R9b</b>	$CO + OH = CO_2 + H$	1.01(8)	0.000	2.50(5)
<b>R4</b>	$OH + OH = H_2O + O$	0.55(11)	0.000	0.29(8)	<b>R9c</b>	$CO + OH = CO_2 + H$	9.03(8)	0.000	1.91(7)
<b>R5</b>	$H + H + M_1 = H_2 + M_1$	1.01(11)	-0.600	0.00	<b>R10</b>	$CO + O + M_1 = CO_2 + M_1$	1.54(9)	0.000	1.25(7)
<b>R6</b>	$H + O + M_2 = OH + M_2$	5.00(11)	-1.000	0.00	<b>R11</b>	$CO + O_2 = CO_2 + O$	2.50(9)	0.000	2.00(8)

Units: m, kmol, s, J

The number in parentheses is the exponent of 10 (for example, 3.82(9) =  $3.82 \times 10^9$ )



and 3800 K. The conditions of freestream at different altitudes are shown in Table 3. Various shock wave structures, including the barrel shock, plume induced shock, and plume boundary, can be observed in Fig. 3. As the elevation gradually increases, the ambient pressure decreases, the Mach number increases and under-expanded plume becomes larger. Also the shock reflection gradually moves away from the nozzle.

Fig. 4 shows the simulated and the measured heating rates at

two calorimeters in the rocket base. The heat flux has two peaks with the maximum values at approximately 10 and 20 km. The simulated results are slightly different with the measured data, since governing equations of the model are discretized by using second-order TVD scheme rather than higher order method. In general, the heating rates show the similar trends. These comparisons suggest that our method can produce accuracy and reliable results for such systems.

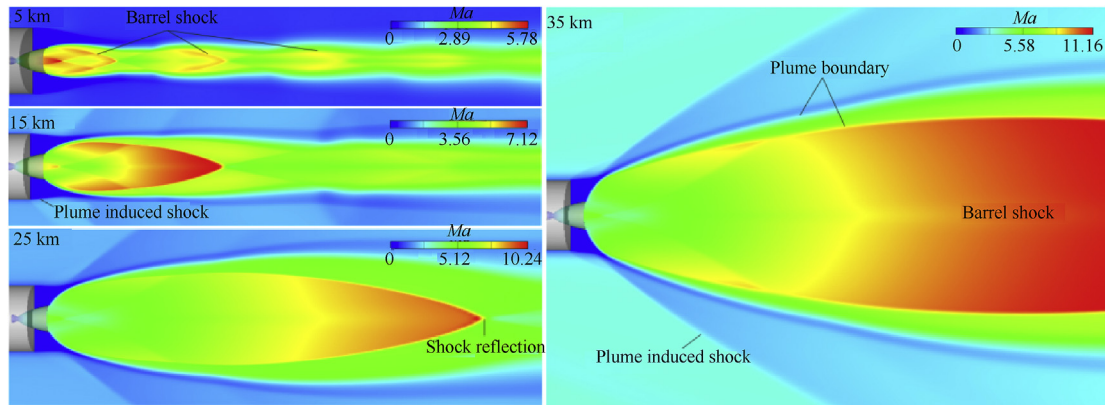


Fig. 3. Contours of Mach number of the liquid rocket exhaust plume at different altitudes.

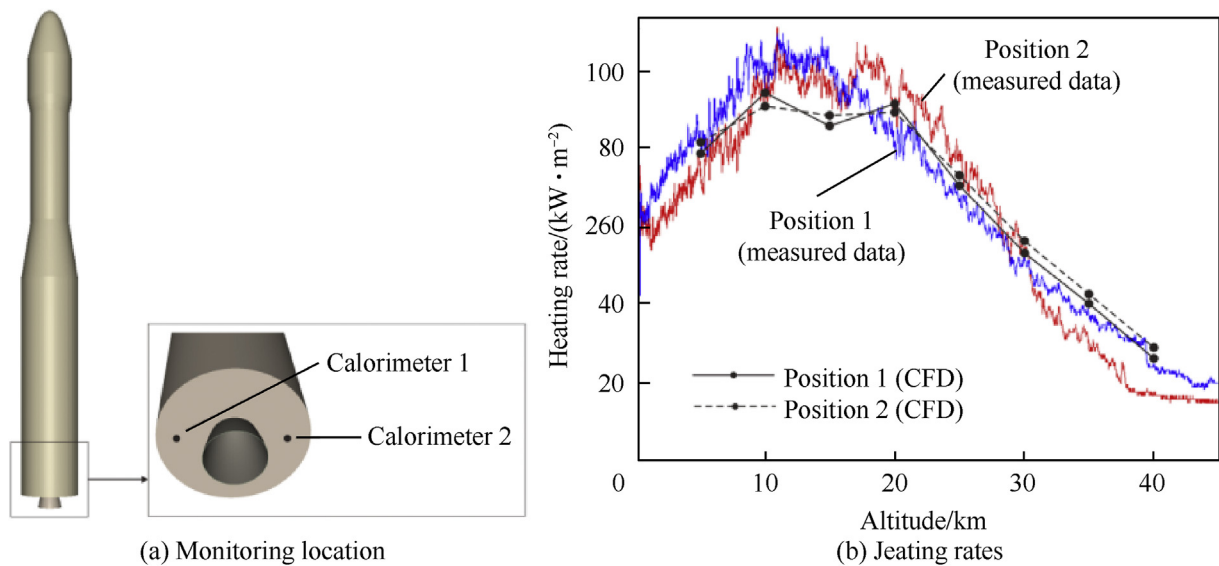


Fig. 4. Comparison of the heating rates between experiments and simulations.

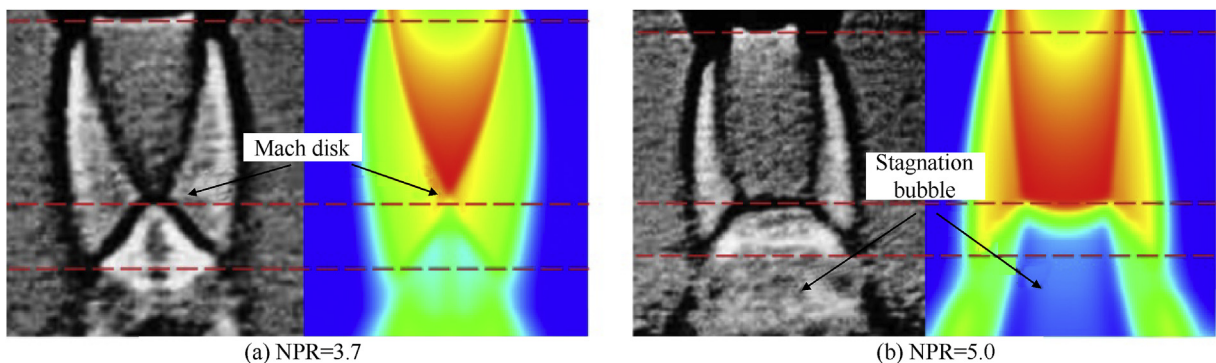


Fig. 5. Flow field contours of different NPR.

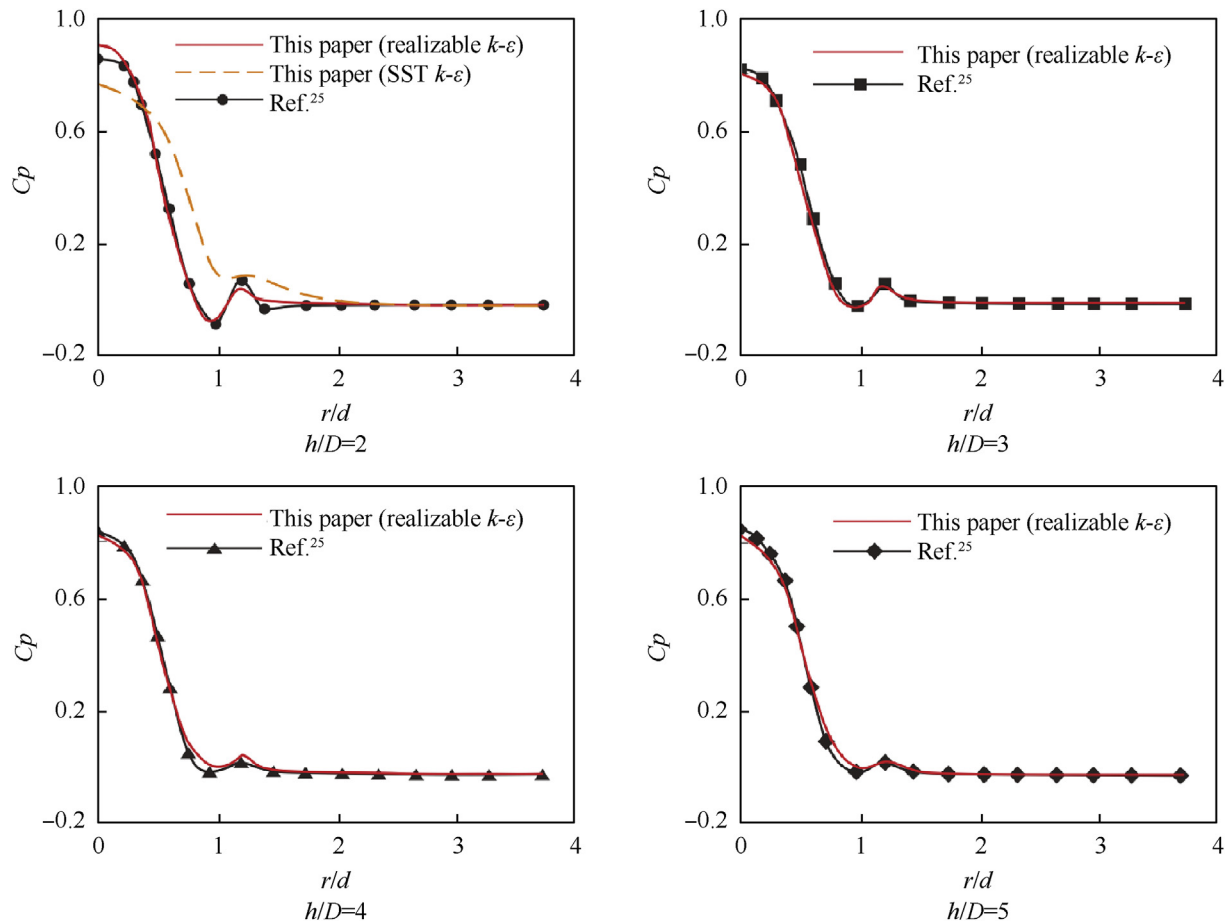


Fig. 6. Comparison of the  $C_p$  distributions on ground plate from measure data [25] and calculation results at different  $h/d$  ratios.

To verify the performance of our model in solving the impact problems, the calculation of sonic jet impingement on the plate is carried out and is compared with the measured data from Alvi and Iyer [25]. The under-expanded supersonic exhaust plume is based on the Laval nozzle with exit diameter ( $D$ ) of 2.54 cm. The nozzle upstream of the throat was designed using a third order polynomial with a contraction ratio of approximately 5. Fig. 5 shows the flow field structure of Ref. [25] (left) and numerical result (right) with different nozzle pressure ratio (NPR) when the distance ( $h$ ) between the ground plate and the nozzle exit is equal to  $2D$ . The contours from numerical simulations are similar to the flow structure in the experiments. For the NPR is 3.7, the surface pressure coefficient ( $C_p$ ) distributions with the change of the radial

location ( $r/D$ ) at  $h/D = 2$  to 5 are shown in Fig. 6. It is show from the case of  $h/D = 2$  that the realizable  $k-\epsilon$  model may get better agreement with the experiment results than the SST  $k-\epsilon$  model. A comparison between the results of calculations with the measured data verifies the reliability and accuracy of the jet impinging model.

## 5. Results and discussion

### 5.1. The exhaust plume flow field

The Mach number, pressure, and temperature contours of the four-engine rockets exhaust plume impinging on the wedge-shaped and cone-shaped deflectors are shown in Figs. 7 and 8.

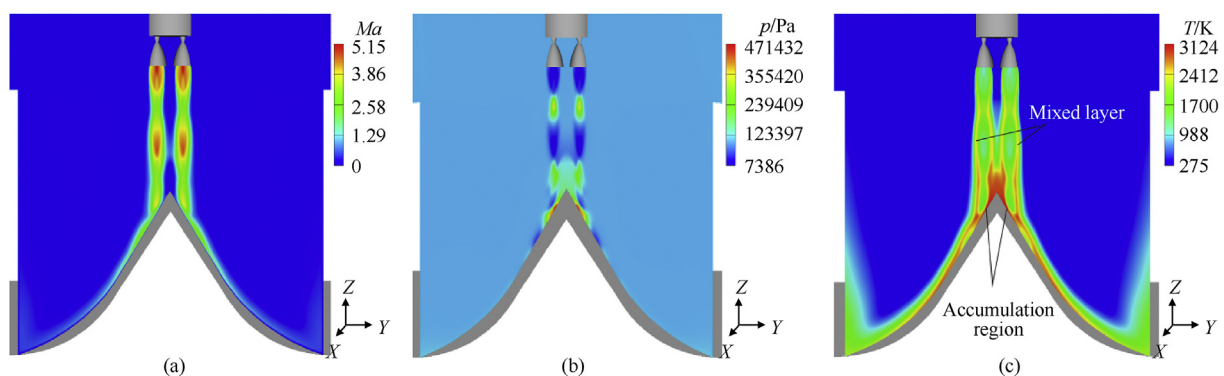


Fig. 7. Mach number (a), pressure (b) and temperature (c) contours of the exhaust plume impinging on the wedge-shaped deflector.

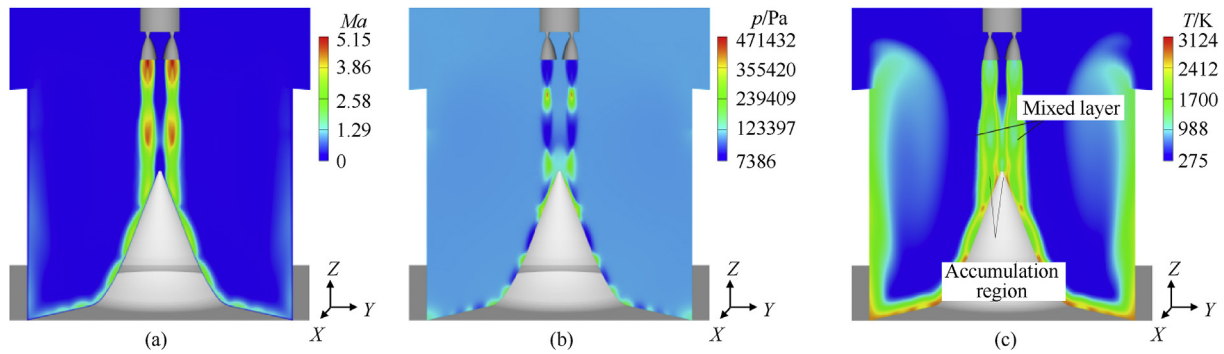
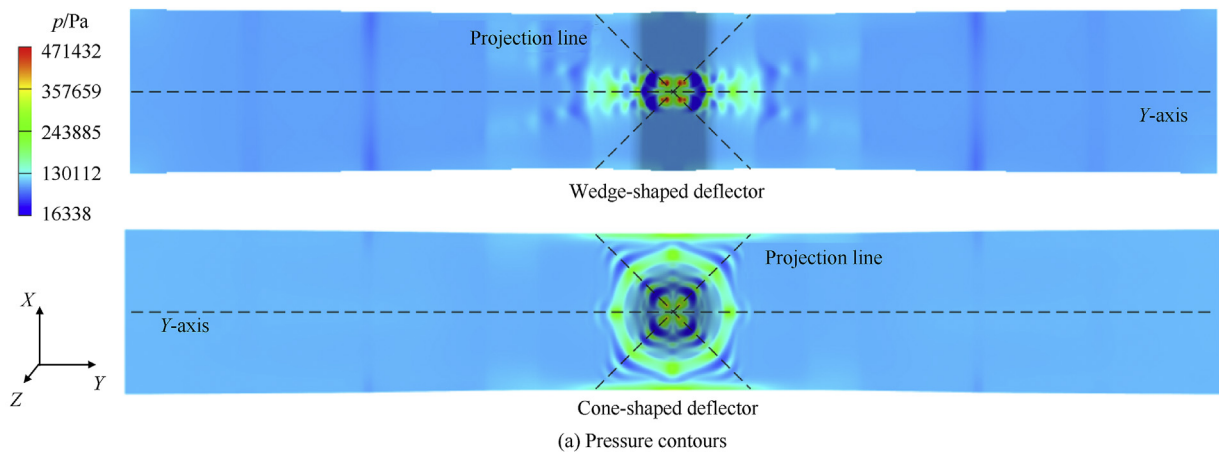


Fig. 8. Mach number (a), pressure (b) and temperature (c) contours of the exhaust plume impinging on the cone-shaped deflector.

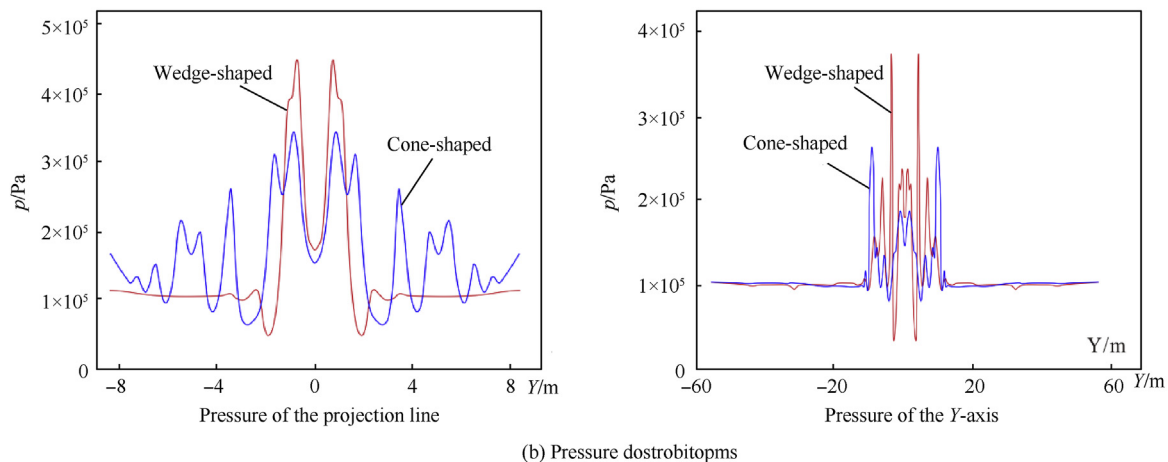
Two symmetry planes are cut off along the axis of nonadjacent nozzle respectively. Three shock cells are formed before the plume impacts the deflector surface. Under the combined effect of external air and high-unexpanded exhaust gas, a clear structure of the first shock cell can be observed near the rocket gas field. But the second shock cell-like structure is less clear due to the interaction of the four equal plumes. The plume radius increases gradually in the lower portions of the second shock cell. The third shock cell deforms after the engine exhaust plumes impact the deflector surface. A high temperature region is generated immediately on the deflector surface due to the impingement and accumulation of

excessive high temperature gas. The core and developed region and boundary of plume are clearly visible downstream of flow field. Due to the afterburning reaction between exhaust gas and air, high temperature also occurs in the mixed layer and average slightly below accumulation region temperature.

As shown by the calculated results, the third shock cell contains a Mach disk, a recirculation region with a wedge or conical shaped to form in front of the plate. Temperature in the accumulation region on the wedge-shaped deflector has increased significantly compared with the cone-shaped deflector. However, due to the restriction of the sidewall of the cone-shaped deflector, part of



(a) Pressure contours



(b) Pressure distribution line charts

Fig. 9. Pressure contours and line charts of the deflector surface.

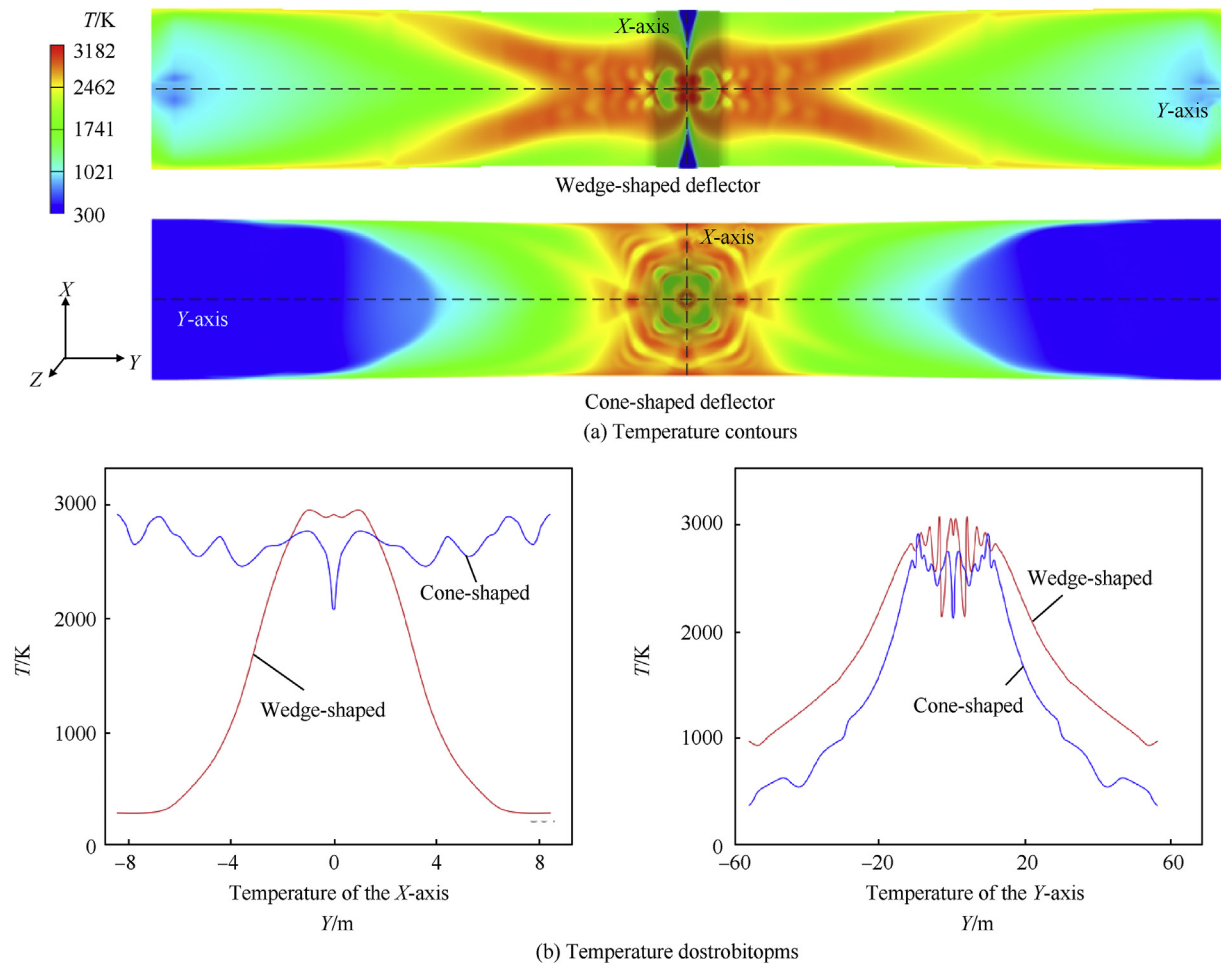


Fig. 10. Temperature contours on the deflector surface (a) and distribution profiles along the X-axis (b).

exhaust gas exits the deflector channel through inlet rather than outlet. Improvements to the cone-shaped deflector design are useful for deflecting exhaust gas smoothly. As the spacing of the sidewalls increases, the cone-shaped deflector could prevent damage to the rocket due to the reverse exhaust plumes.

## 5.2. The impingement surface flow field

Figs. 9 and 10 show the pressure and temperature distribution on the wedge-shaped and cone-shaped deflector surface,

respectively. As expected, the region of peak pressure appears under the rocket nozzle, which is the result of the direct impact of exhaust plume. However, since high velocity of the gas flow is unfavorable for the afterburning reaction, the maximum temperature areas are not formed at the impingement point. The temperature drops gradually from the center to the outlet of the flame deflector. Several cell-like shocks are formed along the plate due to the interaction of four plumes.

As shown in Fig. 9, the wedge-shaped deflector has a peak pressure of 471.4 kPa in the impingement point, well above the

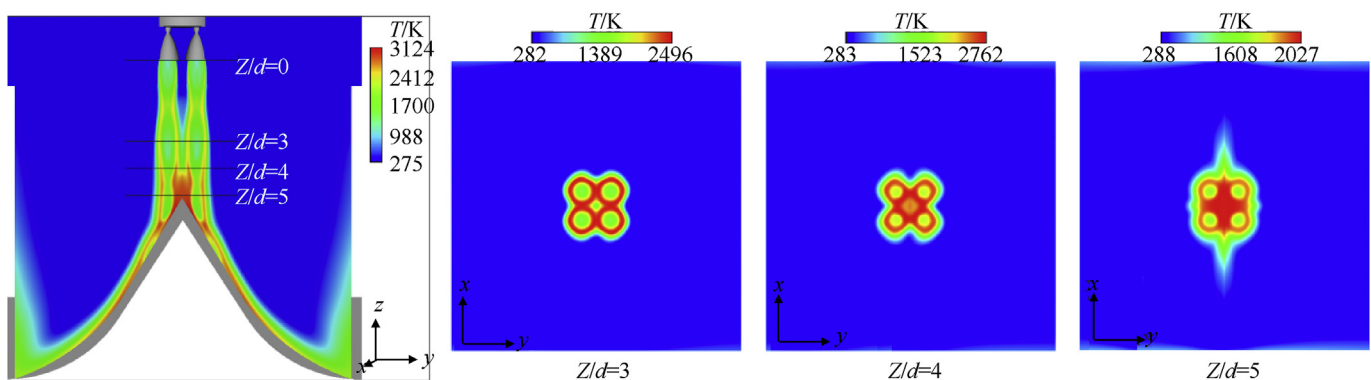


Fig. 11. Planar static temperature contours of the exhaust gas impingement on wedge-shaped deflector.



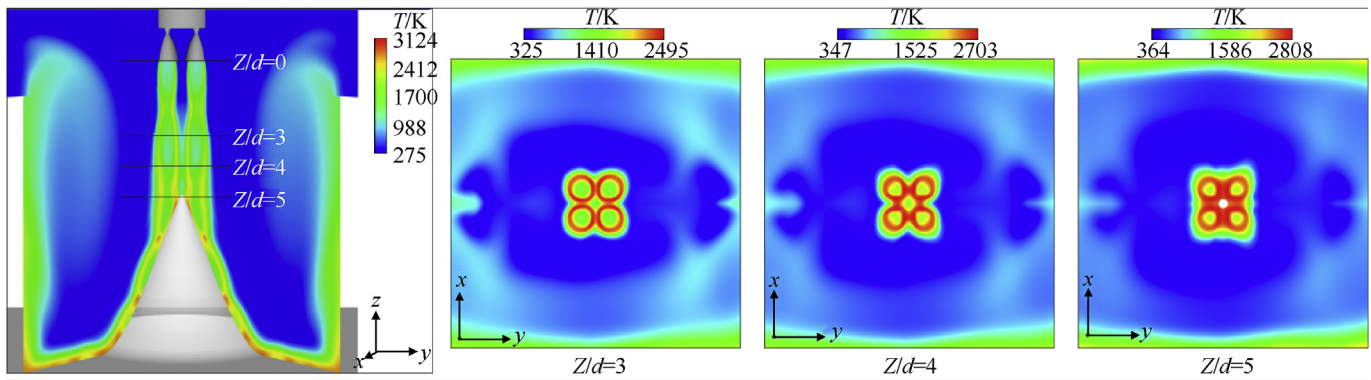


Fig. 12. Planar static temperature contours of the exhaust gas impingement on cone-shaped deflector.

343.5 kPa in the same position on the cone-shaped deflector. Fig. 9(b) displays the pressure distributions along the Y-axis and the projection line which connecting the projection of the nonadjacent nozzle centers on the deflector surface. The pressure changes abruptly in the projection line and Y-axis of the wedge surface. As the conical surface has bigger impact area and better flow capacity, the pressure in the projection line of the wedge surface is higher than those on the conical surface, with the biggest difference about 37.2% at the impingement point.

Fig. 10 displays the temperature distributions on the wedge-shaped and cone-shaped deflector surface, where the maximum values are 3182 K and 2896 K, respectively. Meanwhile, a larger high-temperature region appears in the wedge-shaped deflector. Different diversion orientation of the flame deflectors is a prime cause of the difference in temperature distribution. The supersonic exhaust plume was diverted into outlet with two directions in the wedge-shaped deflector. The high temperature jet impingement on the deflector plate produces large thermal loads and possible ablation on the deflector. On the other hand, the cone-shaped deflector can deflect the exhaust gas towards the circumferential direction, which will cause a smaller thermal shock effect. Fig. 10(b) displays the temperature distributions along the X-axis and Y-axis of the deflector surface. The temperature distribution along the Y-axis of the conical surface is smaller than those in the wedge surface. The high temperature region on the wedge surface is much higher and more focused than in the conical surface, which will more easily lead to a significant ablation and damage in the wedge-shaped deflector. Instead, the wedge plate is underutilized. The conical plate has relatively uniformly distributed in temperature and higher utilization ratio with better anti-ablation performance. One of the weaknesses with the conical plate is that the higher temperature regions occur on both sides of the X-axis. The exhaust gas in the cone-shaped deflector is obstructed by the sidewalls and the obstruction enforces the heating effect at the higher temperature regions. The deflecting performance of the cone-shaped deflector could be improved by reforming the sidewalls structure and increasing the sidewalls spacing.

### 5.3. Planar static temperature contour

Figs. 11 and 12 show the planar static temperature contours for the rocket motor exhaust gas impinging on wedge-shaped and cone-shaped deflectors at  $Z/d = 3, 4$ , and 5 in axial plume direction, where  $Z/d = 0$  corresponds to the nozzle exit. For the supersonic jet impinging on the wedge-shaped deflector, the influence of the plume interaction and exhaust gas circulation are weak since the relatively stable individual shock unit can be observed at  $Z/d = 3$

and 4. The planar static temperature contour at  $Z/d = 5$  is blurred and a circular high temperature region is occurred in the core, which mainly caused by the interaction between exhaust and reverse flow. The exhaust gas inlet of the wedge-shaped deflector has the same temperature as atmosphere except for jet flow region, and not affected by the reverse flow. As shown in Fig. 12, a part of gas flow is discharged from the exhaust gas inlet due to the resistance in sidewalls. The temperature in edge region of planar, as well as the central region, is much higher than ambient temperature. The temperature in the edge at  $Z/d = 3$ , which is closest to the exhaust gas inlet, may reach up to 1000 K. Increasing the distance between the sidewalls of the cone-shaped deflector could be helpful to prevent the damage of the rocket afterbody from high temperature reverse flow.

## 6. Conclusion

Numerical simulations have been performed to investigate the exhaust gas impinging on the wedge-shaped and cone-shaped deflectors. By comparative analysis between the four-engine rockets impinging jet on different deflector, the following conclusions can be made:

- (1) The peak pressure on the deflector surface appears at the intersection of the nozzle axis and the deflector plate, and the temperature drops gradually from the center to the outlet of the deflector.
- (2) The wedge-shaped and cone-shaped deflectors have different diversion directions. The maximum pressure and temperature in the wedge-shaped deflector are, respectively, 37.2% and 9.9% higher than those in the cone-shaped flame deflector.
- (3) Compared to the wedge-shaped deflector, the cone-shaped deflector could achieve better performance for deflecting with sufficient distance of the sidewalls.

### Declaration of competing interest

The authors declare that they have no known competing financial interests or personal relationships that could have appeared to influence the work reported in this paper.

### References

- [1] Lijo V, Kim HD, Setoguchi T, Matsuo S. Numerical simulation of transient flows in a rocket propulsion nozzle. *Int J Heat Fluid Flow* 2010;31:409–17. <https://doi.org/10.1016/j.ijheatfluidflow.2009.12.005>.
- [2] Taghavi SR, Dehnavi MA, Ghafouri A. Numerical analysis of reactive turbulent flow in the thrust chamber of RD-108 engine rocket. *Def Technol* 2019;15:

- 565–75. <https://doi.org/10.1016/j.dt.2018.12.004>.
- [3] Donahue BB, Weldon VA, Paris SW. Low recurring cost, partially reusable heavy lift launch vehicle. *J Spacecraft Rockets* 2008;45:90–4. <https://doi.org/10.2514/1.29313>.
  - [4] Ebrahimi HB, Levine J, Kawasaki A. Numerical investigation of twin-nozzle rocket plume phenomenology. *J Propul Power* 2000;16:178–86. <https://doi.org/10.2514/2.5572>.
  - [5] Desikan S, Suresh K, Saravanan R, Chandrasekar N, Patil M, Pandian S. Effect of freestream-plume interaction on launch vehicle aerodynamics coefficients with different flared aft-bodies. *Exp Therm Fluid Sci* 2017;53:354–69. <https://doi.org/10.1016/j.expthermflusci.2016.09.006>.
  - [6] Hwayoung O, Jungil L, Hyungsik U, Hwanil H. Numerical study for flame deflector design of a space launch vehicle. *Adv Space Res* 2017;59:1833–47. <https://doi.org/10.1016/j.asr.2016.12.038>.
  - [7] Zhang J, Qu Z, Fu R, He Y. Experimental study on the transient thermal characteristics of an integrated deflector under the periodic impingement of a supersonic flame jet. *Int J Heat Mass Tran* 2015;58:811–23. <https://doi.org/10.1016/j.ijheatmasstransfer.2015.02.031>.
  - [8] Nallasamy R, Kandula M, Duncil L, Schallhorn P. Numerical simulation of the base flow and heat transfer characteristics of a four-nozzle clustered rocket engine. In: 40th Thermophysics Conf; 2008. <https://doi.org/10.2514/6.2008-4128>.
  - [9] Chen B, Gao R, Liang Y, Zhao J, Sun Y. Experimental investigation of atomization and droplet turbulence characteristics of a twin-fluid nozzle with different self-excited vibrating cavity structures. *Exp Therm Fluid Sci* 2018;99: 525–36. <https://doi.org/10.1016/j.expthermflusci.2018.08.017>.
  - [10] Jiang C, Han T, Gao Z, Lee C. A review of impinging jets during rocket launching. *Prog Aero Sci* 2019;109(100574). <https://doi.org/10.1016/j.paerosci.2019.05.007>.
  - [11] Moraes P, Morgenstren A. Evaluation of the effectiveness of VLS launcher flame deflector. *Comput Fluids* 2001;30(5):523–32. [https://doi.org/10.1016/S0045-7930\(01\)00003-2](https://doi.org/10.1016/S0045-7930(01)00003-2).
  - [12] Zhang X, Chen H. Numerical study on similarity of plume infrared radiation between reduced-scale solid rocket motors. *Chin J Aeronaut* 2016;29:924–33. <https://doi.org/10.1016/j.ast.2010.09.006>.
  - [13] Brehm C, Sozer E, Moini-Yekta S, Housman JA, Kiris C, Barad MF, Vu BT, Parlied CR. Computational prediction of pressure environment in the flame trench with launch vehicles. In: 31st AIAA Applied Aerodynamics Conf; 2013. <https://doi.org/10.2514/6.2013-2538>.
  - [14] Tatsukawa T, Nonomura T, Oyama A, Fujii K. Multi-objective aeroacoustic design exploration of launch-pad flame deflector using large-eddy simulation. *J Spacecraft Rockets* 2016;53:751–8. <https://doi.org/10.2514/1.A33420>.
  - [15] Akamine M, Okamoto K, Gee KL, Neilsen TB, Teramoto S, Okunuki T, Tsutsumi S. Effect of nozzle-plate distance on acoustic phenomena from supersonic impinging jet. *AIAA J* 2018;56:1–10. <https://doi.org/10.2514/1.J056504>.
  - [16] Daniel C, Vineet A. Computational plume modeling of conceptual ARES vehicle stage tests. In: 43rd AIAA/ASME/SAE/ASEE Joint Propulsion Conf. and Exhibit; 2007. <https://doi.org/10.2514/6.2007-5708>.
  - [17] Sachdev JS, Ahuja V, Hosangadi A, Daniel C. Analysis of flame deflector spray nozzles in rocket engine test stands. In: 46th AIAA/ASME/SAE/ASEE Joint Propulsion Conf. and Exhibit; 2010. <https://doi.org/10.2514/6.2010-6972>.
  - [18] Tsutsumi S, Takaki R, Nakanishi Y, Okamoto K, Teramoto S. Acoustic generation mechanism of a supersonic jet impinging on deflectors. In: 52nd Aerospace Sciences Meeting; 2014. <https://doi.org/10.2514/6.2014-0882>.
  - [19] Oh H, Lee J, Um H, Huh H. Numerical study for flame deflector design of a space launch vehicle. *Adv Space Res* 2017;59:1833–47. <https://doi.org/10.1016/j.asr.2016.12.038>.
  - [20] Vatsa VN, Wedan BW. Development of a multigrid code for 3-D Navier-Stokes equations and its application to a grid-refinement study. *Comput Fluids* 1990;18:391–403. [https://doi.org/10.1016/0045-7930\(90\)90029-w](https://doi.org/10.1016/0045-7930(90)90029-w).
  - [21] Shih TH, Liou WW, Shabbir A, Yang Z, Zhu J. A new k-ε eddy viscosity model for high Reynolds number turbulent flows. *Comput Fluids* 1995;24:227–38. [https://doi.org/10.1016/0045-7930\(94\)00032-t](https://doi.org/10.1016/0045-7930(94)00032-t).
  - [22] Frey AE, Tien JS. A theory of flame spread over a solid fuel including finite-rate chemical kinetics. *Combust Flame* 1979;36:263–89. [https://doi.org/10.1016/0010-2180\(79\)90064-6](https://doi.org/10.1016/0010-2180(79)90064-6).
  - [23] Saxena P, Williams FA. Testing a small detailed chemical-kinetic mechanism for the combustion of hydrogen and carbon monoxide. *Combust Flame* 2006;145:316–23. <https://doi.org/10.1016/j.combustflame.2005.10.004>.
  - [24] Jensen DE, Jones GA. Reaction rate coefficients for flame calculations. *Combust Flame* 1978;32:1–34. [https://doi.org/10.1016/0010-2180\(78\)90078-0](https://doi.org/10.1016/0010-2180(78)90078-0).
  - [25] Alvi F, Iyer K. Mean and unsteady flowfield properties of supersonic impinging jets with lift plates 5th AIAA/CEAS Aeroacoustics Conf. 1999. <https://doi.org/10.2514/6.1999-1829>.